Binghamton University

# The Open Repository @ Binghamton (The ORB)

Mechanical Engineering Faculty Scholarship

Mechanical Engineering

5-2020

# Towards a high bias voltage MEMS filter using electrostatic levitation

Mark Pallay
*Binghamton University--SUNY*, mpallay1@binghamton.edu

Ronald Miles
*Binghamton University--SUNY*, rmiles@binghamton.edu

Shahrzad Towfighian
*Binghamton University--SUNY*, stowfigh@binghamton.edu

## Recommended Citation

# Towards A High Bias Voltage MEMS Filter using Electrostatic Levitation

Mark Pallay[a], Ronald N. Miles[a], Shahrzad Towfighian[a],*

[a]*Mechanical Engineering Department, Binghamton University*
*Binghamton, New York, 13902 USA*

## Abstract

Traditional MEMS filters use a comb drive structure that suffers from the pull-in instability, which places a significant limitation on the achievable signal-to-noise ration of the sensor. Because the output signal from a capacitive sensor is linearly related to the applied voltage, it is desirable to use a capacitive sensor that can withstand large voltages upwards of 100V. However, the pull-in instability causes high voltages to destroy the device and a trade-off between performance and reliability must be made. Electrostatic levitation, which works by pulling electrodes apart instead of together, eliminates the pull-in instability and allows for very high voltages to be applied without damaging or destroying the sensor/actuator. This study theoretically and experimentally demonstrates that a filter based on electrostatic levitation eliminates the voltage limitation of the capacitive sensor, which has historically hampered the performance of the filter. A model of the filter is derived and validated with experimental data. Voltages up to 100V are applied without damaging the filter.

*Keywords:* MEMS, Filter, Electrostatic Levitation, High Voltage

## 1. Introduction

Signal filtering is an extremely important process in many electronic systems. Filters remove unwanted frequency components from a signal such as

---

*Corresponding author
*Email address:* `stowfigh@binghamton.edu` (Shahrzad Towfighian)

those coming from environmental noise, nonlinearities in the system, or other
signals. This can be a critical when analyzing a signal or passing it to another
component, because in many cases signals may be heavily distorted from noise
such that no useful information can be extracted from them. Filtering can be
accomplished in many different ways. The first filters were made with simple
electronic circuts using resistors, inductors, and capacitors [1]. Filters can also
be constructed with vibrating mechanical systems or with microprocessors integrated in electrical circuits. Each type of filter has its own advantages and
disadvantages. Digital filters, while having the potential to outperform analog
filters, are much more complex and require a microprocessor, which adds delay
and consumes external power. Analog filters, such as electrical and mechanical
filters, are much less complex and require little to no input power. However,
their performance can be hindered by environmental changes such as temperature and fabrication imperfections. They also have other undesirable attributes
such as passband rippling and roll-off [1]. Ultimately, the application dictates
what type of filter is the most suitable, which is why both analog and digital
filters are commonly used in many commercial products.

Electromechanical filters have been widely studied since the 1940s. These
filters utilize a resonating structure to filter out frequencies that are sufficiently
far from the natural frequency of the system [2]. Typically, they consist of an
electrically controlled actuator that is moving in response to an input signal.
This motion is either mechanically or electrically transferred to a second structure (a sensor), which has its motion converted back to an electrical signal.
If the input signal is near the natural frequency, it will cause the actuator to
resonate, which will be transferred to the sensor and produce a large output
signal. If the input is away from a natural frequency, the actuator does not resonate, and therefore the output signal from the sensor is significantly smaller.
This filtering process exploits fundamental phenomenon of coupled oscillating
structures [3, 4] and requires very little input power to operate. This is ideal
for applications such as wireless transmitters and receivers that benefit from
advantages of passive filters, which are very stable, cheap to manufacture, and

2

easy to integrate in an electrical system.

Initially, electromechanical filters had numerous disadvantages because of their cost and size. With the advent of metal-oxide-semiconductor (MOS) technology, switch-capacitor filters overtook electromechancial filters because they could be miniaturized and incorporated into single-chip systems [5]. Some effort had been placed into creating very small electromechanical filters as early as the 1960s [6] because of the potential for tunability and low energy loss (high quality (Q) factor)[7, 8]. However, the reliability of these filters were problematic and could not be addressed at the time.

With advances in the micromachining process for microelectromechanical systems (MEMS), micromechanical filters were brought back into the spotlight in the early 1990s because the issues of reliability and low Q factors could be addressed. As early as 1992, Lin et. al. fabricated MEMS filters that used resonance of mechanically coupled comb-drive oscillators to create band-pass filters with a high degree of tunability and the potential for very large quality factors if operated in a vacuum [5]. The filters were operated by actuating one comb-drive with an input voltage signal. The motion was transferred through a weak coupling spring to a second comb-drive. This motion was detected with a capacitive sensor. However, the quality factor was relatively low because the devices were operated in air. The filter was subsequently redesigned in 1998 to be vacuum sealed and in this case quality factors of up to 2200 were achieved [9]. High quality factors produce very a sharp roll-off at the edge of the passband, which is very desirable for filters.

Since then, capacitive MEMS filters have been further developed to obtain large Q factors, higher center frequencies, and more frequency tunability [10, 11, 12, 13, 14]. Nearly all MEMS filters use an electrode configuration that is analogous to a parallel-plate capacitor. This is the most common form of a capacitive sensor because it produces a large capacitance, which creates a lot of output signal. However, these devices are susceptible to the pull-in instability if a large voltage is applied to the sensor.

Pull-in occurs when the applied voltages causes the two electrodes to col-

3

lapse and stick together. If the electrodes are stuck there will be no change in capacitance and the sensor will not work. This is a major limiting factor in electrostatic MEMS and is usually designed around at the expense of performance. In an ideal capacitive sensor, a very large voltage would be applied to boost the amount of output signal. Pull-in limits the maximum applied voltage and, in turn, the total output signal the sensor can produce. Since the voltage is limited, to increase the output, the capacitance can be increased by using a comb-drive structure. However, increasing the capacitance also increases the electrostatic force and lowers the pull-in threshold. Therefore, to get an optimal signal out of a capacitive sensor the voltage and capacitance need to be balanced.

One method of avoiding the pull-in instability is to use an alternative arrangement of electrodes that induces electrostatic levitation [15, 16, 17, 18, 19, 20, 21, 22]. Instead of pulling two electrodes together, electrostatic levitation pulls two electrodes apart. A cross section of the electrode configuration is shown in Figure 1. This arrangement was first proposed in [16], and consists of three electrodes fixed to a substrate with a fourth movable electrode (a beam) suspended directly above the center fixed electrode. When a voltage is applied to the side electrodes, the electric field pulls on the top of the beam more than the bottom, and there is a net force upwards. The beam and center electrode are kept at the same voltage and are not pulled together, so there is no pull-in instability. There is a small possibility of a side instability of the beam, but if the aspect ratio of the cross section is high such that it has a high in-plane stiffness and a low out-of-plane stiffness, pull-in will not occur even if hundreds of volts are applied to the side electrodes.

The elimination of the pull-in instability with electrostatic levitation is very desirable for both electrostatic actuators and capacitive sensors. For actuators, the actuation distance can be orders of magnitude larger than the anchor height, whereas in traditional parallel-plate systems the beam motion is limited to one third of the initial gap or less. For capacitive sensors, the voltage is not limited by the pull-in instability anymore, and tremendously high voltages can be applied to boost the output signal. The authors have previously obtained dis-

4

placements of almost $25\mu$m with a MEMS cantilever that has an anchor height of just $2\mu$m. In the same study, 195V was applied to the side electrodes with no pull-in failure or electrical damage to the device [18].
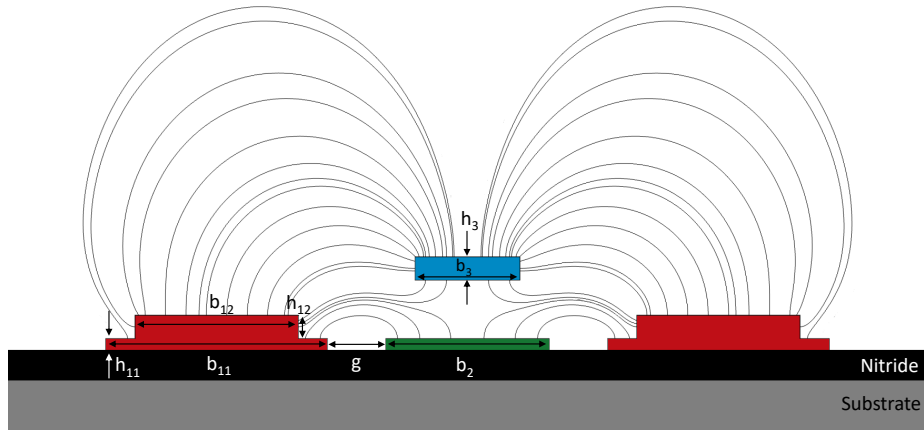


Figure 1: Electrode configuration for electrostatic levitation with cantilever beam (blue), fixed center electrode (green), and fixed side electrodes (red).

<sub>100</sub> In this study, a MEMS filter based on electrostatic levitation is introduced. The filter has a similar structure to previous MEMS filters with a coupled actuator and sensor, except it uses the electrostatic levitation electrode arrangement. It can be supplied with very high voltages because of the eliminated pull-in instability. The high actuating voltage creates a large amplitude resonance of the <sub>105</sub> actuator, which increases the change in capacitance of the sensor. The sensing voltage can also be increased significantly to boost the output signal. The advantage of this design is it does not have a theoretical limit on the amplitude of the signal it can produce. If more signal is desired, a higher sensing voltage can be applied and it should not negatively affect the dynamics of the filter.

<sub>110</sub> The contribution of this study is to demonstrate the feasibility and advantages of electrostatic actuation and capacitive sensing with electrostatic levitation for the purpose of signal filtering. The filter is not limited by the trade off between applied voltage and capacitance, which hinders the performance of its parallel-plate counterpart. This can be very useful for any capacitive sensor

5

or actuator that is limited by the pull-in instability. In Section 2 the design of the filter is outlined. Section 3 derives a theoretical model of the system. The experimental setup and methods are discussed in Section 4. In Section 5 the results are discussed and analyzed. Finally, some concluding remarks are given in Section 6.

## 2. Filter Design

The filter consists of two cantilever beams with the electrostatic levitation arrangement in Figure 1. The two beams are connected with a serpentine coupling spring at the node of the cantilevers second mode. The beams, electrodes, and coupling spring are made of polysilicon and deposited on a $0.5\mu$m thick layer of silicon nitride to insulate them from the bulk silicon. The structure of the filter is shown in Figure 2, and the dimensions are given in Table 1.

The filter is designed to use the second natural frequency of the cantilevers as the passband. One very important characteristic of coupled oscillators, such as this filter, is that they have "symmetric" and "asymmetric" modes and natural frequencies. Because the actuating and sensing beam have the same geometry and are made of the same material, they should have identical natural frequencies (ignoring fabrication imperfections). The symmetric modes are when both beams are oscillating at the same natural frequency and are in phase with each other. In this case, the motion of the actuator and sensor are identical and the coupling spring remains undeformed. The asymmetric modes are when both beams are moving at the same frequency, except they are 180 degrees out of phase. Now, the coupling spring is deformed and adds more stiffness to the system. Therefore, the asymmetric mode has a higher natural frequency than the asymmetric modes. If the coupling spring is placed at a node of a given mode, the asymmetric natural frequency will be very close to the symmetric frequency, which is desirable for filters to minimize passband rippling. The desired mode for the filter dictates where the coupling spring is located, which is why it is placed at the node of the second mode. The second mode is chosen

6

Table 1: Beam parameters as shown in Figure 1

| Parameter | Symbol | Value |
|---|---|---|
| Cantilever Length | $L_1$ | $350\mu$m |
| Beam Width | $b_3$ | $18\mu$m |
| Beam Thickness | $h_3$ | $1.5\mu$m |
| Beam Anchor Height | $d$ | $2.75\mu$m |
| Electrode Side Gap | $g$ | $5\mu$m |
| Center Electrode Width | $b_2$ | $28\mu$m |
| Side Electrode Layer 1 Width | $b_{11}$ | $38\mu$m |
| Side Electrode Layer 2 Width | $b_{12}$ | $28\mu$m |
| Side Electrode Start | $E_{si}$ | $10\mu$m |
| Side Electrode End | $E_{ei}$ | $263\mu$m |
| Electrode Layer 1 Thickness ($\mu$m) | $h_{11}$ | $0.5\mu$m |
| Electrode Layer 2 Thickness ($\mu$m) | $h_{12}$ | $2\mu$m |
| Elastic Modulus | E | 160GPa |
| Density | $\rho$ | 2330 $^{kg}/_{m^3}$ |
| Poisson's Ratio | $\nu$ | 0.22 |
| Coupling Spring Location | $L_c$ | $274.2\mu$m |
| Coupling Spring Width | $b_c$ | $3\mu$m |
| Coupling Spring Length 1 | $L_{c1}$ | $70\mu$m |
| Coupling Spring Length 2 | $L_{c2}$ | $7\mu$m |
| Coupling Spring Length 3 | $L_{c3}$ | $30\mu$m |
| Number of Spring Turns | $n$ | $5\mu$m |

instead of the first mode to increase the frequency of the passband. According to a finite-element analysis of the filter model in Figure 2, the second symmetric and asymmetric natural frequencies are 103kHz and 105kHz respectively. The second asymmetric mode is shown in Figure 3.

One drawback of using the second mode is that the amplitude is much smaller than the first mode. To mitigate this issue, partial side electrodes are used to boost the response of the second mode. It has been previously demonstrated that the use of partial electrodes can be used to increase the amplitude of specific modes if placed properly [23]. The height of the side electrodes is also increased (Figure 1) to boost the strength of the levitation force and further increase the amplitude.

The electrical connections for the filter are slightly more complicated than they are for a single isolated beam. Previously, the authors would ground the beam and center electrode, and superimpose an AC and DC voltage on the side electrodes to create electrostatic levitation [18, 19]. However, this can not be done in this case because the filter requires a separate actuating signal and sensing voltage. Furthermore, the coupling spring is made from polysilicon, which electrically connects the actuating and sensing beams. It is also important that the input signal is completely isolated from the output signal so it does not feed into the capacitive sensor either directly or through electrostatic induction. A cross-section of the actuating and sensing electrodes with electrical connections are shown in Figure 4.

The sensor and actuator each have three electrodes; 1) the side electrodes (treated as a single electrode), 2) the center fixed electrode, and 3) the beams. As mentioned above, the beams are electrically connected together through the coupling spring and must be the same voltage as the center fixed electrode for electrostatic levitation. The input signal must be applied to the side electrodes of the actuator. If it was applied to the beam or center electrode, it would travel to the capacitive sensor through the coupling spring and would not be filtered. For a similar reason, the output signal must come from the sensor side electrodes to avoid any influence from the input signal through electrostatic induction on

8

the beam and center electrode. The sensing voltage is applied to the beam and center electrode and serves multiple purposes. Most importantly, it provides a voltage for the capacitive sensor. It also acts as the DC component for the input signal on the actuator. This will significantly boost the actuator response, which will generate a larger capacitance change of the sensor and more output signal. Lastly, it acts as an electrical shield between the input and output signal. If the actuator and sensor side electrodes are sufficiently far from each other, the only electrical path from the input signal to the output signal is through the beam and center electrode. The voltage source for $V_{sense}$ keeps the voltage on the beam and center electrode constant, and prevents any signal from the input from passing through it.

Another complicating factor of this filter is that the multi-electrode sensor creates multiple capacitances between each pair of electrodes. Figure 5 shows this problem with the equivalent circuit diagram of the filter. Because the actuator and sensor act like two connected loops of capacitors, it is impossible to isolate a single capacitance to sense. However, the circuit diagram can be reduced to simplify the electrical problem. In the same way that the side electrodes were treated as a single electrode because they are always given the same voltage, the beam and center electrode can also be treated as a single electrode. This simplifies the capacitance network into a simple set of two capacitors in series for the entire filter. In Figure 5, $C_{23a}$ and $C_{23s}$ are removed because they have the same voltage on either side. Then, for the actuator, $C_{13a}$ and $C_{12a}$ are two capacitors in parallel, which can be summed into a single capacitor $C_a$, and a similar process can be performed with the sensor to give a single capacitor $C_s$. The simplified filter circuit connected with a charge amplifying circuit is shown in Figure 6.

The circuit in Figure 6 is much easier to analyze. The simplified filter circuit in the red box has just two capacitors and a single voltage source. The other resistors, capacitor, and op-amp act as a charge amplifying circuit and are commonly used with capacitive sensors to obtain an electrical readout. If $R_f$ is sufficiently large, the output of the charge amplifier ($V_{out}$) can be expressed by,

9

$$V_{out} = \frac{C_s V_{sense}}{C_f} \tag{1}$$

Eq. (1) shows why increasing the sensing voltage boosts the output of the sensor. Because pull-in is eliminated, $V_{sense}$ can be increased to hundreds or thousands of volts to boost the output signal. In conventional MEMS filters, such as a comb drive filter, $V_{sense}$ is limited by the lateral pull-in voltage. Comb drive filters mitigate this issue by increasing the number of comb fingers to increase the capacitance, $C_s$, which also has a linear relationship with $V_{out}$. However, adding more fingers increases the size, which increases bulk manufacturing costs, and adds mass, which lowers the natural frequency and causes the filter to be more susceptible to inertial forces that could distort the output. The levitating filter does not need to make these trade-offs to increase the output signal, because $V_{sense}$ can be increased until the output reaches a satisfactory level.

## 3. Model Derivation

To model the filter, Hamilton's principle can be used. Hamilton's principle is a variational problem based on the principle of least action and is expressed by,

$$\int_{t1}^{t2} [\delta T - \delta V + \delta W_{ex}] \, dt = 0 \tag{2}$$

where $\delta T$ is the variational kinetic energy, $\delta V$ is the variational potential energy, and $\delta W_{ex}$ is the virtual work of external forces. To use Hamilton's principle, all relevant energies of the system must be quantified. The relevant energy terms are given in Eqs. (3)-(7).

$$T_{beam} = \frac{1}{2} \int_0^L \left[ \rho_1 A_1 \dot{w}^2 H\left(L_1 - x\right) + \rho_2 A_2 \dot{w}^2 H\left(x - L_1\right) \right] dx \tag{3}$$

$$V_{beam} = \frac{1}{2} \int_0^L \left[ E_1 I_1 w_{xx}^2 H\left(L_1 - x\right) + E_2 I_2 w_{xx}^2 H\left(x - L_1\right) \right] dx \tag{4}$$

10

$$V_{spring} = \frac{1}{2}k_{ct}\left(w(L_{cs}, t) - w(L_{ca}, t)\right)^2 + \frac{1}{2}k_{cr}\left(w_x(L_{cs}, t) - w_x(L_{ca}, t)\right)^2 \quad (5)$$

$$\delta W_{elec} = \int_{E_{s1}}^{E_{e1}} \left[V_s^2 f_e \delta w H\left(L_1 - x\right)\right] dx + \int_{E_{s2}}^{E_{e2}} \left[V_a^2 f_e \delta w H\left(x - L_1\right)\right] dx \quad (6)$$

$$\delta W_{sqfd} = \int_0^L \left[-c_1 \dot{w} \delta w H\left(L_1 - x\right) - c_2 \dot{w} \delta w H\left(x - L_1\right)\right] dx \quad (7)$$

where $T_{beam}$ and $V_{beam}$ are the kinetic and bending strain energy of the beam respectively, $V_{spring}$ is the strain energy of the coupling spring from bending and twisting, $\delta W_{elec}$ is the virtual work from the electrostatic force ($f_e$), $\delta W_{sqfd}$ is the virtual work from squeeze film damping, $w$ is the transverse deflection of the beam, $L$ is the total length of the x-domain, $L_{cs}$ is the location of the coupling spring on the sensing beam, $L_{ca}$ is the location of the coupling spring on the actuating beam $V_s$ and $V_a$ are the voltages applied to the sensor and actuator respectively, $k_{ct}$ and $k_{cr}$ are the transnational and rotational stiffness of the coupling spring, and $H(x)$ is the Heaviside step function. The kinetic energy of the spring is ignored because it is placed at a node. This means it should stay relatively still and only bend/twist for the asymmetric second mode. The electrostatic force, $f_e(w)$, is calculated in COMSOL and fit with a fifth order polynomial.

The x-domain runs along the length of each beam. From Figure 2, each beam has the same x-domain and are separated by a short distance in the y-direction. However, to simplify the problem and avoid introducing another variable, $y$, into the problem, the x-domain is defined to run from the anchor to the tip of the sensing beam before jumping to the anchor of the actuating beam. The domain will be discontinuous at this point, but this is resolvable by establishing a different set of boundary conditions at this point that depends on the direction it is approached from. This will yield a total of eight boundary conditions, with four for each beam. There will also be four constraints at the intersection of the coupling spring and beam (eight total). These state the

11

beam displacement and slope are continuous, and the shear force and moment are balanced at this point. The total x-domain length, $L$, is twice the beam lengths, $L_1$. In the energy terms from Eqs. (3)-(7), the Heaviside step function is used to differentiate between each beam.

Taking the variation of Eqs. (3)-(5) and plugging everything into Eq. (2) yields the boundary conditions, constraints, and governing equation of motion [Eq. (8)]. The details of this procedure are outlined in the Appendix.

$$H(x - L_1) \left[ \rho_1 A_1 \ddot{w} + c_1 \dot{w} + E_1 I_1 w_{xxxx} \right.$$
$$\left. - V_s^2 \sum_{j=0}^{5} \beta_j w^j \right] + H(L_1 - x) \left[ \rho_2 A_2 \ddot{w} + c_2 \dot{w} + \right.$$
$$\left. E_2 I_2 w_{xxxx} - V_a^2 \sum_{j=0}^{5} \beta_j w^j \right] = 0 \quad (8)$$

where $\beta_i$ are the fitting coefficients for the electrostatic force. Eq. (8) has two partial differential equations (PDE) separated by the Heaviside step function. The first PDE governs the motion of the sensing beam and the second PDE governs the motion of the actuating beam. These PDEs must adhere to the boundary conditions and constraints derived during Hamilton's principle. One small simplification that can be made to the governing equation is to set $\rho_1 = \rho_2 = \rho$, $A_1 = A_2 = A$, etc. This can be done because the beams are assumed to be identical and therefore have the same material properties and geometry.

Eq. (8) is nondimensionalized with the substitutions shown in Eq. (9).

$$\hat{w} = \frac{w}{h_3} \qquad \hat{x} = \frac{x}{L} \qquad \hat{t} = \frac{t}{T} \qquad T = \sqrt{\frac{\rho A L^4}{EI}} \qquad (9)$$

The governing equation is reduced into a set of coupled ordinary differential equations (ODE) using Galerkin's method. This assumes the beam response can be represented as a linear combination of space dependent components, $\phi_i(x)$, called mode shapes, multiplied by time dependent components, $\eta_i(t)$. For the filter, the first four modes are considered, which corresponds to the first

12

and second symmetric and asymmetric modes.

$$\hat{w}(\hat{x}, \hat{t}) = \sum_{i=1}^{4} \phi_i(\hat{x}) \eta_i(\hat{t}) \tag{10}$$

The mode shapes are determined by solving the eigenvalue problem of Eq. (8) using the boundary conditions and constraints. This is performed numerically in COMSOL using finite-element analysis. Eq. (10) is plugged into the nondimensionalied Eq. (8) yielding,

$$H(\hat{x} - L_1) \left( \sum_{i=1}^{4} \phi_i \ddot{\eta}_i + \frac{c}{EIT} \sum_{i=1}^{4} \phi_i \dot{\eta}_i + \right.$$

$$\left. \sum_{i=1}^{4} \phi_{i_{xxxx}} \eta_i - V_s^2 \sum_{j=0}^{5} \frac{L^4 \beta_j h_3^{j-1}}{EI} \left[ \sum_{i=1}^{4} \phi_i \eta_i \right]^j \right) +$$

$$H(L_1 - \hat{x}) \left( \sum_{i=1}^{4} \phi_i \ddot{\eta}_i + \frac{c}{EIT} \sum_{i=1}^{4} \phi_i \dot{\eta}_i + \right.$$

$$\left. \sum_{i=1}^{4} \phi_{i_{xxxx}} \eta_i - V_s^2 \sum_{j=0}^{5} \frac{L^4 \beta_j h_3^{j-1}}{EI} \left[ \sum_{i=1}^{4} \phi_i \eta_i \right]^j \right) = 0 \tag{11}$$

Next, Eq. (11) is multiplied by $\phi_k$ and integrated over the x-domain. This exploits the orthogonality condition of the mode shapes and decouples linear terms. The orthogonality condition states,

$$\int_{x_1}^{x_2} \phi_i \phi_k dx = 0 \qquad i \neq k \tag{12}$$

where $x_1$ and $x_2$ are the boundaries of the domain. When Eq. (11) is multiplied by $\phi_k$ and integrated over $\hat{x}$, the only terms that remain are the linear terms with $\phi_i$ when $i = k$ and the nonlinear terms in the electrostatic force. If this process is repeated for $k = 1, 2, 3, 4$, it results in four coupled nonlinear ODEs in time, which are shown in Eq. (13).

$$\ddot{\eta}_k + c_k \dot{\eta}_k + \lambda_k^4 \eta_k - \sum_{i=0}^{5} \alpha_{jk} \left( V_s^2 \int_{E_{s1}}^{E_{e1}} \phi_k \left[ \sum_{i=1}^{4} \phi_i \eta_i \right]^j d\hat{x} \right.$$

$$\left. + V_a^2 \int_{E_{s2}}^{E_{e2}} \phi_k \left[ \sum_{i=1}^{4} \phi_i \eta_i \right]^j d\hat{x} \right) = 0 \tag{13}$$

13

where

$$\alpha_{jk} = \frac{L^4 \beta_j h_3^{i-1}}{EI m_k} \qquad m_k = \int_0^1 \phi_k^2 dx \qquad c_k = \frac{\lambda_k^2}{Q} \tag{14}$$

and $\lambda_k^2$ is the $k^{th}$ natural frequency, and Q is the quality factor.

Eq. (13) is very difficult to solve efficiently. The nonlinear electrostatic force requires a numerical solution technique, and the four mode expansion inside the fifth order polynomial makes efficient numerical techniques, such as shooting method and harmonic balance, very difficult and tedious to implement. This requires Eq. (13) to be integrated many times to obtain a frequency response, which is very computationally inefficient. However, if the input signal is small, the frequency response will be linear and the electrostatic force can be linearized. If the force is linear, Galerkin's method will result in four uncoupled linear ODEs that can be solved analytically. This allows the solution to be obtained almost instantly.

In this pursuit, the electrostatic force is linearized about its static equilibrium position using a Taylor Series. The nonlinear Eq. (13) can not be avoided completely because it is still needed to find the static position of the beam, but this can be done easily. The time dependent terms are dropped and a solution in the form of a constant ($C_k$) can be substituted in for $\eta_k$. This gives four coupled algebraic equations for $C_k$, which can be solved very quickly using Newton-Raphson's method.

Once the static solution, $\hat{s}$, is known, the electrostatic force can be rewritten as,

$$f_e(\hat{w}) = \sum_{j=0}^{5} \beta_j h_3^j \hat{w}^j \approx \gamma_0 + \gamma_1 \hat{w} \tag{15}$$

where

$$\gamma_0 = \sum_{j=0}^{5} (1-j)\beta_j h^j \hat{s}^j \qquad \gamma_1 = \sum_{j=0}^{5} j\beta_j h^j \hat{s}^{j-1} \tag{16}$$

Replacing the fifth order polynomials in Eq. (8) with Eq. (15), and repeating Galerkin's method yields,

$$\ddot{\eta}_k + c_k \dot{\eta}_k + \lambda_k^4 \eta_k - V_s^2 (A_{0k} + A_{1k}\eta_k) - V_a^2 ((B_{0k} + B_{1k}\eta_k) = 0 \tag{17}$$

where

$$A_{ik} = \frac{L^4 h_3^{i-1} \gamma_i}{EIm_k} \int_{E_{s1}}^{E_{e1}} \phi_k^2 d\hat{x} \qquad B_{ik} = \frac{L^4 h_3^{i-1} \gamma_i}{EIm_k} \int_{E_{s2}}^{E_{e2}} \phi_k^2 d\hat{x} \qquad (18)$$

Eq. (17) can be solved analytically with the method of undetermined coefficients. The sensor voltage, $V_s$ is given a constant voltage between 50V and 100V. The actuator voltage is a harmonic input signal superimposed on a DC voltage. The DC voltage is the same as $V_s$ because of the wiring diagram shown in Figure 4. The actuator frequency is stepped across the second symmetric and asymmetric natural frequency to obtain the frequency response of the filter.

## 4. Experimental Setup and Methods

The filters are fabricated with PolyMUMPs standard fabrication [24]. The electrodes and beams are made in polysilicon, which are insulated from the bulk silicon with a $0.6\mu$m thick silicon nitride layer. An image of a fabricated filter is shown in Figure 7. To characterize the filter behavior, the dynamic response of the filter is examined. The experimental set up to characterize the frequency response of the filters is shown in Figure 8. The filters are place in a vacuum chamber and the pressure is reduced to around 400mTorr. A National Instruments USB 6366 data acquisition system (DAQ) sends an AC signal to the side electrodes of the actuator. A Krohn-Hite 7600 amplifier supplies a DC voltage of 50V-100V to the beams and center electrodes. Instead of running the sensor electrodes into a charge amplifying circuit like shown in Figure 6, these electrodes are grounded. A Polytec MSA 500 laser vibrometer measures beam tip velocity and sends the data back to the DAQ.

The input signal to the actuator side electrodes is a stepped sine function that sweeps across the second symmetric and asymmetric natural frequencies of the filter. Because the MSA 500 is a single point vibrometer, this experiment is performed twice to measure the actuator and sensor tip velocities. The experimental data is compared to the results of the linear model, which are found using the method of undetermined coefficients.

15

Table 2: Beam parameters as shown in Figure 1

| Mode | FEA Model | Experiment |
|------|-----------|------------|
| 1st symmetric | 14.79kHz | 12.23kHz |
| 1st asymmetric | 26.79kHz | 21.11kHz |
| 2nd symmetric | 102.84kHz | 83.52kHz |
| 2nd asymmetric | 104.55kHz | 84.86kHz |

## 5. Results and Discussion

Before the frequency response is obtained, the natural frequencies of the
fabricated filters are extracted. The FEA model predicts a the second natural
frequencies should be around 100kHz, however fabrication imperfections will
inevitably affect these values. Therefore, a small white noise signal is placed
on the side electrodes of the actuator and the beam tip velocity is measured.
A fast-Fourier transform (FFT) is applied to the velocity signal to view the
frequency spectrum. There will be large spikes at the natural frequencies of the
system. An FFT of the beam velocity is shown in Figure 9 and the extracted
natural frequencies are given in Table 2.

In Figure 9, there is some low frequency noise, which is ignored, and five
spikes in the frequency spectrum. The lower two, around 12kHz and 21kHz are
the first symmetric and asymmetric natural frequencies of the filter. They are
far apart because the coupling spring is not located near the node of the first
mode, and therefore adds a significant amount of stiffness to the system for the
asymmetric mode. The highest two are the second symmetric and asymmetric
natural frequencies. These are very close together, which is desirable for filters
to minimize passband rippling. There is a fifth spike around 78kHz, which
was not considered in the theoretical model outlined in Section 3. This is the
resonant frequency of the coupling spring. It was previously assumed that the
effective mass of the spring was negligible because it is located at a node and
should have almost no kinetic energy. While this is a good assumption when

16

driving the system near its second natural frequencies, it is important to not stray too far from this point so the assumption does not become invalid.

It is apparent in Table 2 that the FEA predicted natural frequency is about 20% higher than it is in the experiment. There are several reasons why this is the case. First, there is some compliance of the support, which is not accounted for in the model. The lower anchoring stiffness causes a decrease in the natural frequency. The beam is not completely flat either. There is a small dip in the beam near the anchor, which can be seen in Figure 7. This happens because the center electrode does not run all the way to the anchor of the beam. This was done to keep the beam and center electrode electrically disconnected on the chip so a separate voltage could be applied to the beam if desired. Lastly, the actual thickness of the beams was found to be slightly less than the intended 1.5$\mu$m. These imperfections cause the actual natural frequency to be notably lower than the predicted natural frequency for a perfect beam. To account for this, the natural frequencies from the experiment are inserted in the model for $\lambda_k^2$ to account for these defects.

Next, the stepped frequency sweep is conducted. The frequency responses at 0.75$V_{AC}$ for DC voltages ($V_{sense}$) of 50V, 75V, and 100V are shown in Figure 10. The model and experiment show excellent agreement with each other. As the DC voltage is increased, the mechanical response of the filter is not negatively affected. The natural frequencies increase slightly with DC voltage, but more importantly the amplitude also increases. So not only does an increase in voltage boost the electrical output according to Eq. (1), it also boosts the mechanical response. This is a very promising result as the increase in voltage does not have the downside of instability like it does in a parallel-plate capacitive sensor/actuator.

The next step would be to obtain an electrical readout of the filter. However, an issue with the parasitic resistance and parasitic capacitance through the silicon nitride becomes problematic in this case. One important part of the PolyMUMPs fabrication procedure is the deposition of a thin silicon nitride layer that is used to isolate the electrodes from the bulk silicon and from each

other. While silicon nitride can have a very high resistivity in the GΩm range [25], it still acts as a parasitic resistor that runs in parallel with the actuator and sensor capacitors in Figure 6 ($C_a$ and $C_s$). If the resistance of the nitride is much larger than the impedance of the capacitors, it will not be problematic. But for the filter, the impedance of the sensor is too large (i.e. the capacitance is very small), and an electrical readout of the filter is not possible. To demonstrate this, the total capacitiance between center electrode/beam and side electrodes is calculated in COMSOL (Figure 11).

One very surprising attribute of the levitating system is the increase in capacitance as the beam moves upward, away from the side electrodes. It is expected that as the beam moves away from the other electrodes, the capacitance should decrease. However, with a levitating structure this is not the case. When the beam is very close to the center electrode, the bottom face of the beam, and the top face of the center electrode are "shielded" from the side electrodes as there is only a very thin layer of air between them that the electric field can travel through. As the beam moves upward, the bottom face becomes more visible to the side electrodes. At the deflected position, more of the electric field from the side electrodes can reach the beam because the bottom face is now exposed, and the capacitance is increased. If the beam is pulled very far away from the side electrodes, eventually the capacitance will fall back down again, but this does not occur in the range of gaps the filter is realistically capable of achieving, so for this system it can be stated that the capacitance increases with gap.

The nominal capacitance of $C_s$ is very small. The average capacitance per unit length in Figure 11 is around 25fF/mm. Since the beams are approximately 0.35mm long, this gives a nominal capacitance of less than 10fF. When driven at 80kHz, the impedance of $C_s$ is roughly 1.5GΩ. The effective resistance of the nitride can be measured with a Keithley electrometer and is found to be just 160MΩ, which is an order of magnitude lower than the impedance of the sensor and actuator. This means the circuit diagram in Figure 6 effectively has a resistor across capacitors $C_a$ and $C_s$, which connects the input signal and sensing voltage to the inverting input of the op-amp. There is also notable par-

18

asitic capacitance through the silicon nitride to the polysilicon substrate, which gives the input signal another route to bypass the capacitive sensor, $C_s$. This results in a considerable DC component of the op-amp output (from $V_{sense}$) and a significant portion of the input signal bypassing the filter. While the DC component can be eliminated by applying a small voltage to the non-inverting input of the op-amp, the leakage of the input signal can not be mitigated because it is at the same frequency as the desired signal output. Because of these issues, an electrical readout could not be obtained in the experiment using the PolyMUMPs fabrication procedure. This problem can be mitigated by depositing a more effective isolation layer between the electrodes and bulk silicon, such as 1-2$\mu$m of silicon dioxide.

Despite the issue with obtaining an electrical readout of the filter experimentally, the sensor output can be estimated theoretically using the capacitance data in Figure 11. The beam tip displacement for each mode is extracted from the model and multiplied with the corresponding mode shape. All four modes are summed to give the profile of the deformed beam. The beam deflection at each point along the beam can be used with the capacitance data in Figure 11 to get the capacitance per unit length, which can be integrated along the portion of the sensor beam that is adjacent to the side electrodes to get the total capacitance. The peak-to-peak change in capacitance can be used with Eq. (1) to estimate the peak-to-peak voltage output of the capacitive sensor when hooked up to the charge amplifying circuit in Figure 6. The frequency response of the calculated peak-to-peak output signal is shown in Figure 12.

The output signal frequency response shows an increase in output voltage with sensing voltage. At $50V_{DC}$ the output is just 4.3mV at the resonant peaks and quickly drops below 0.1mV when away from resonance. The dynamic amplitude of the beam at the resonant peak for $50V_{DC}$ is only 0.6$\mu$m, which corresponds to a change in capacitance of about 0.09fF. To account for the very small capacitance, the sensing voltage can be increased to boost the output signal. Doubling the sensing voltage to 100V doubles the dynamic amplitude to 1.27$\mu$m at the resonant peak, which corresponds to a change in capacitance of

19

0.17fF and an output voltage of 17.6mV. By doubling the sensing voltage, the sensor output is quadrupled because it boosts both the dynamic response of the beam, which increases the capacitance, and the output of the capacitive sensor according to Eq. (1).

A 17.6mV output signal from a 0.75V input correlates to an insertion loss of approximately 32.6dB, which is significantly larger than most other MEMS filters that have insertion losses in the 2-8dB range [26, 27]. However, with a 0.1pF feedback capacitor and a bias voltage of 441V, the output of the filter can be boosted up to 0.75V (assuming the change in capacitance is around 0.17fF as it is for the case of 100V bias), which has virtually no signal loss from the input. The levitating structure is designed to withstand voltages in this range, so creating a zero-loss MEMS filter using this structure should be possible.

In some applications, applying 441V is not feasible, which would make using this filter unrealistic if the desire is to have no loss of signal. To reduce the voltage needed for a zero-loss filter, a similar tactic that is used in comb drives to increase the capacitance can be used in the levitation filter. Many fingers can be added to the capacitive sensor to increase capacitance, and reduce the required bias voltage. In previous studies, a microphone [28] and accelerometer [29] were made using this concept and provided readable output signals from a levitating capacitive sensor. A similar approach can be used for the filter, although this comes at the cost of increase the size.

While the the total output signal is still relatively small for the voltage levels , the results show that the output signal can be boosted by increasing the sensing voltage without the possibility of triggering pull-in.


## 6. Conclusion

In this study a capacitive MEMS filter that uses electrostatic levitation is introduced. This filter can be supplied with very high voltages because it does not suffer from the pull-in instability. 100V was applied to the filter without failure or mechanical damage. The high voltage boosts the output of the filter

by increasing the dynamic amplitude of the actuating beam and increasing the charge induced on the sensing electrodes of the sensor. Doubling the applied voltage quadrupled the output voltage of the sensor because of these two effects. This is very promising for MEMS filters and all capacitive sensors that have their performance hampered by the pull-in instability by removing the voltage limitation. It is also promising for capacitive filters in high voltage applications, demonstrating they can be miniaturized to sizes that are similar to their low voltage counterparts.

## 7. Acknowledgment

**Appendix**

Hamilton's principle is frequently used to derive the governing equations of motion for dynamic systems. However, another advantage of Hamilton's principle is that boundary conditions and constraints for continuous systems can be derived as well. This happens naturally when evaluating Eq. (2) and will be outline here.

First, the variation of the kinetic and potential energies given in Eqs. (3)-(5) are evaluated. The variation can be seen like a derivative and is calculated in a very similar way. These are shown in Eqs. (19)-(21). For simplicity, the evaluations are only carried out for the sensor beam (beam 1). These are identical for the actuating beam and are not shown here.

$$\delta T_{beam} = \int_0^L \left[ \rho_1 A_1 \dot{w} \delta \dot{w} H \left( L_1 - x \right) + ... \right] dx \tag{19}$$

$$\delta V_{beam} = \int_0^L \left[ E_1 I_1 w_{xx} \delta w_{xx} H \left( L_1 - x \right) + ... \right] dx \tag{20}$$

$$\delta V_{spring} = k_{ct}(w(L_{cs}, t) - w(L_{ca}, t)) \times (\delta w(L_{cs}, t) - \delta w(L_{ca}, t)) + \\ k_{cr}(w_x(L_{cs}, t) - w_x(L_{ca}, t)) \times (\delta w_x(L_{cs}, t) - \delta w_x(L_{ca}, t)) \tag{21}$$

21

Eqs. (19)-(21) are plugged into Eq. (2) and coefficients of $\delta w$, $\delta \dot{w}$, $,\delta w_x$, and $\delta w_{xx}$ are grouped together. However, both $\delta \dot{w}$ and $\delta w_{xx}$ can be transformed into $\delta w$ by using integration by parts on the time $(dt)$ and spatial $(dx)$ integral respectively. This is shown in Eqs. (22) and (23) for one term each.

$$\int_{t_1}^{t_2} \left[ \int_0^{L_1} (\rho_1 A_1 \dot{w} \delta \dot{w}) \, dx \right] dt =$$
$$\int_0^{L_1} (\rho_1 A_1 \dot{w} \delta w) \, dx \Big|_{t_1}^{t_2} - \tag{22}$$
$$\int_{t_1}^{t_2} \left[ \int_0^L (\rho_1 A_1 \ddot{w} \delta w) \, dx \right] dt$$

$$\int_{t_1}^{t_2} \left[ \int_0^{L_1} (E_1 I_1 w_{xx} \delta w_{xx}) \, dx \right] dt =$$
$$\int_{t_1}^{t_2} \left[ E_1 I_1 w_{xx} \delta w_x \Big|_0^{L_1} - E_1 I_1 w_{xxx} \delta w_x \Big|_0^{L_1} + \tag{23} \right.$$
$$\left. \int_0^{L_1} E_1 I_1 w_{xxxx} \delta w \, dx \right] dt$$

In Eqs. (22) and (23), the terms inside both the time and spatial integral that are multiplied by $\delta w$ are used to derive the governing equation of motion [Eq. (8)]. For Hamilton's principle all the remaining terms must be equal to zero. These terms can be used to derive the boundary conditions and constraints, with the exception of the second term in Eq. (22), which is zero because both $\delta w(t_1)$ and $\delta w(t_2)$ are zero. The boundary conditions are shown in Eqs. (24) amd 25).

$$w(0,t) = w_x(0,t) = w_{xx}(L_1^-,t) = w_{xxx}(L_1^-,t) = 0$$
$$w(L_1^+,t) = w_x(L_1^+,t) = w_{xx}(L,t) = w_{xxx}(L,t) = 0 \tag{24}$$

$$w(L_{cs}^-, t) - w(L_{cs}^+, t) = w_x(L_{cs}^-, t) - w_x(L_{cs}^+, t) = 0$$

$$w(L_{ca}^-, t) - w(L_{ca}^+, t) = w_x(L_{ca}^-, t) - w_x(L_{ca}^+, t) = 0$$

$$E_1 I_1 \left( w_{xxx}(L_{cs}^-, t) - w_{xxx}(L_{cs}^+, t) \right) + k_{ct} \left( w(L_{cs}, t) - w(L_{ca}, t) \right) = 0$$

$$E_1 I_1 \left( w_{xx}(L_{cs}^-, t) - w_{xx}(L_{cs}^+, t) \right) + k_{cr} \left( w_x(L_{cs}, t) - w_x(L_{ca}, t) \right) = 0 \qquad (25)$$

$$E_2 I_2 \left( w_{xxx}(L_{ca}^-, t) - w_{xxx}(L_{ca}^+, t) \right) + k_{ct} \left( w(L_{ca}, t) - w(L_{cs}, t) \right) = 0$$

$$E_2 I_2 \left( w_{xx}(L_{cs}^-, t) - w_{xx}(L_{cs}^+, t) \right) + k_{cr} \left( w_x(L_{ca}, t) - w_x(L_{cs}, t) \right) = 0$$

In Eqs. (24) and (25) the + and - superscript refers to the direction that the point is approached from. There are 16 total boundary conditions, which includes 8 constraints at the ends of the coupling spring. These equations are used to solve the eigenvalue problem for the mode shapes and natural frequencies. However, for simplicity the eigenvalue problem is solved using FEA in COMSOL and all subsequent integrals in the model analysis are calculated numerically.

## Acknowledgment

## References

## References

[1] K. L. Su, Analog filters, Springer Science & Business Media, 2012.

[2] R. A. Johnson, Mechanical filters, CRC Handbook of Electrical Filters (1997) 377.

[3] W. B. Case, P. J. Tjossem, K. G. Abrams, J. F. St. Germaine-Fuller, Coupled oscillators driven with difference-frequency parametric position feedback, Journal of Applied Physics 122 (12) (2017) 124905.

[4] D. K. Agrawal, J. Woodhouse, A. A. Seshia, Synchronization in a coupled architecture of microelectromechanical oscillators, Journal of Applied Physics 115 (16) (2014) 164904.

23

[5] L. Lin, C. T.-C. Nguyen, R. T. Howe, A. P. Pisano, Microelectromechanical filters for signal processing, Proceedings of IEEE Micro Electro Mechanical Systems (1992) 226–231.

[6] H. C. Nathanson, W. E. Newell, R. A. Wickstrom, J. R. Davis, The resonant gate transistor, IEEE Transactions on Electron Devices 14 (3) (1976) 117–133.

[7] K. Ekinci, M. Roukes, Nanoelectromechanical systems, Review of scientific instruments 76 (6) (2005) 061101.

[8] X. Liu, J. Vignola, H. Simpson, B. Lemon, B. Houston, D. Photiadis, A loss mechanism study of a very high q silicon micromechanical oscillator, Journal of Applied Physics 97 (2) (2005) 023524.

[9] L. Lin, R. T. Howe, A. P. Pisano, Microelectromechanical filters for signal processing, Journal of Microelectromechanical Systems 7 (3) (1998) 286–294.

[10] K. Wang, C. T.-C. Nguyen, High-order medium frequency micromechanical electronic filters, Journal of Microelectromechanical Systems 8 (4) (1999) 534–557.

[11] A.-C. Wong, C. T.-C. Nguyen, Micromechanical mixer-filters ("mixlers"), Journal of Microelectromechanical Systems 13 (1) (2004) 100–112.

[12] M. Motiee, R. R. Mansour, A. Khajepour, Novel mems filters for on-chip transceiver architecture, modeling and experiments, Journal of Micromechanics and Microengineering 16 (2) (2006) 407–418.

[13] M. Hajhashemi, A. Amini, B. Bahreyni, A micromechanical bandpass filter with adjustable bandwidth and bidirectional control of centre frequency, Sensors and Actuators A 187 (2012) 10–15.

[14] M. A. A. Hafiz, L. Kosuru, A. Z. Hajjaj, M. I. Younis, Highly tunable narrow bandpass mems filter, IEEE Transactions of Electron Devices 64 (8) (2017) 3392–3398.

24

[15] K. B. Lee, Y. H. Cho, Laterally driven electrostatic repulsive-force microactuators using asymmetric field distribution, Journal of Microelectromechanical Systems 10 (1) (2001) 128–136. `doi:10.1109/84.911101`.

[16] S. He, R. Ben Mrad, Large-stroke microelectrostatic actuators for vertical translation of micromirrors used in adaptive optics, IEEE Transactions on Industrial Electronics 52 (4) (2005) 974–983.

[17] C. Fan, S. He, A Two-Row Interdigitating-Finger Repulsive-Torque Electrostatic Actuator and Its Application to Micromirror Vector Display, Journal of Microelectromechanical Systems 24 (6) (2015) 2049–2061. `doi:10.1109/JMEMS.2015.2467389`.

[18] M. Pallay, M. Daeichin, S. Towfighian, Dynamic Behavior of an Electrostatic MEMS Resonator with Repulsive Actuation, Nonlinear Dynamics 89 (2) (2017) 1525–1538. `doi:10.1007/s11071-017-3532-z`.

[19] M. Pallay, S. Towfighian, A parametric electrostatic resonator using repulsive force, Sensors and Actuators A: Physical 277 (2018) 134 – 141. `doi:10.1016/j.sna.2018.04.001`.

[20] M. Ozdogan, M. Daeichin, A. Ramini, S. Towfighian, Parametric Resonance of a Repulsive Force MEMS Electrostatic Mirror, Sensors and Actuators A Physical, 265 (2017) 20–31. `doi:10.1016/j.sna.2017.07.043`.

[21] M. Pallay, R. N. Miles, S. Towfighian, Merging parallel-plate and levitation actuators to enable linearity and tunability in electrostatic mems, Journal of Applied Physics 126 (1) (2019) 014501.

[22] M. Pallay, A. I. Ibrahim, R. N. Miles, S. Towfighian, Pairing electrostatic levitation with triboelectric transduction for high-performance self-powered mems sensors and actuators, Applied Physics Letters 115 (13) (2019) 133503.

[23] J. Nizar, A. Ramini, A. A. Carreno, M. I. Younis, Higher order modes excitation of electrostatically actuated clamped–clamped microbeams: ex-

25

perimental and analytical investigation, Journal of Micromechanics and

<sub>545</sub> Microengineering 26 (2) (2016) 025008.

[24] A. Cowen, B. Hardy, R. Mahadevan, S. Wilcenski, PolyMUMPs Design
Handbook a MUMPs®️ process (2011).
URL `http://www.memscap.com/__data/assets/pdf_file/0019/1729/`
`PolyMUMPs-DR-13-0.pdf`

<sub>550</sub> [25] O. Lukianova, A. Khmara, S. Perevislov, D. Kolesnikov, V. Krasilnikov,
Electrical resistivity of silicon nitride produced by various methods, Ce-
ramics International 45 (7) (2019) 9497–9501.

[26] K. Entesari, G. M. Rebeiz, A 12-18-ghz three-pole rf mems tunable filter,
IEEE Transactions on microwave theory and techniques 53 (8) (2005) 2566–
<sub>555</sub> 2571.

[27] A. Abbaspour-Tamijani, L. Dussopt, G. M. Rebeiz, Miniature and tunable
filters using mems capacitors, IEEE Transactions on Microwave Theory
and Techniques 51 (7) (2003) 1878–1885.

[28] M. Ozdogan, S. Towfighian, R. Miles, A mems microphone with repulsive
<sub>560</sub> sensing, The Journal of the Acoustical Society of America 141 (5) (2017)
3793–3793.

[29] M. Daeichin, M. Ozdogan, S. Towfighian, R. Miles, Dynamic response of a
tunable mems accelerometer based on repulsive force, Sensors and Actua-
tors A: Physical 289 (2019) 34–43.

26
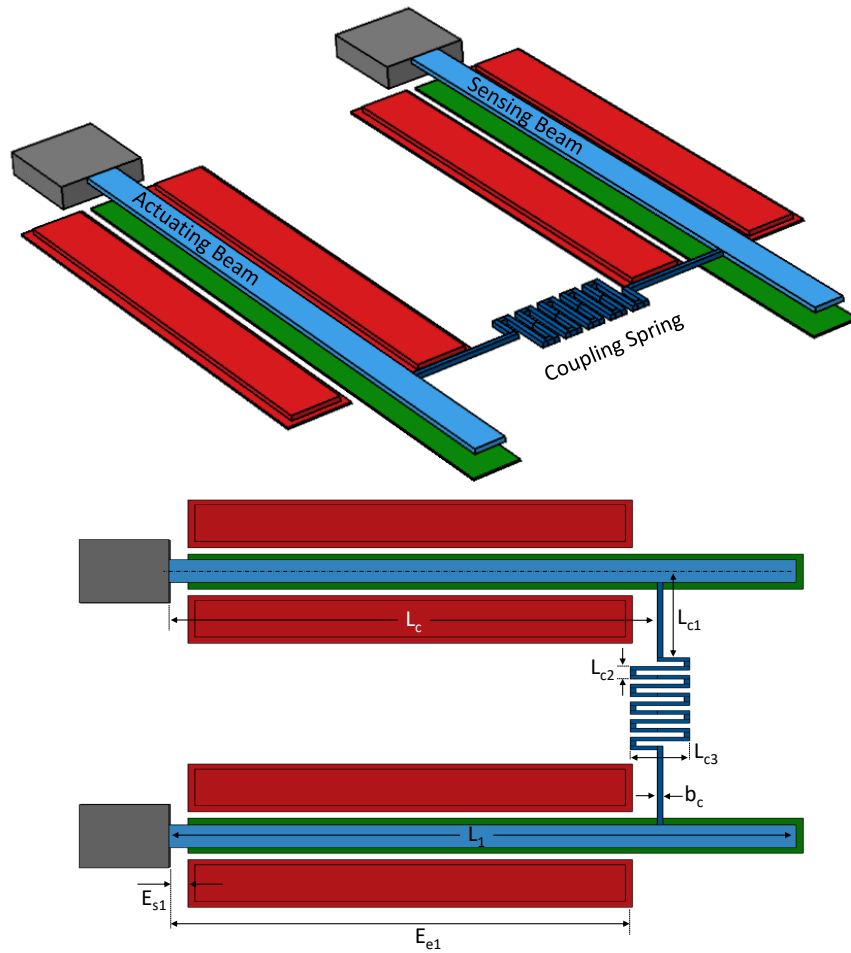
Figure 2: Layout of the filter with geometric parameters.
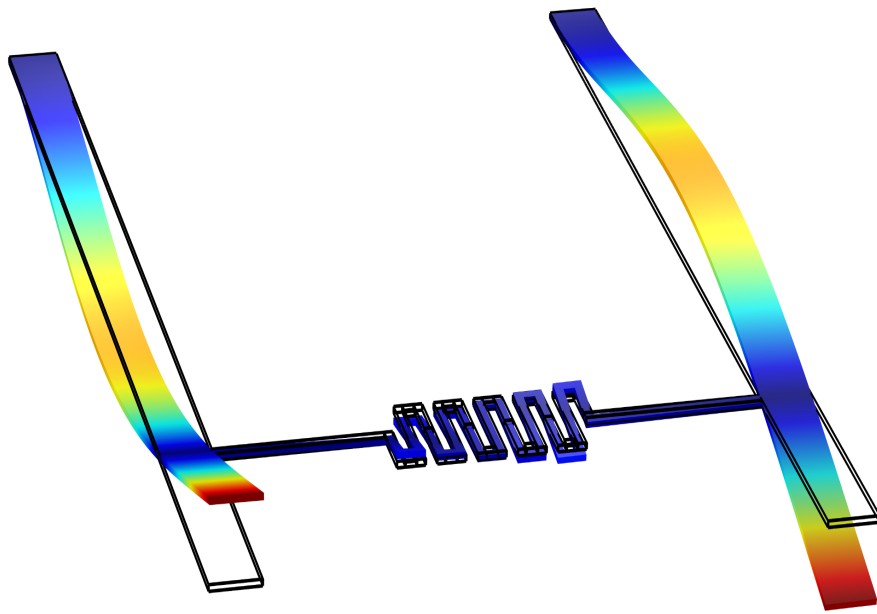
Figure 3: The second asymmetric mode shape calculated in COMSOL. The solid black lines show the undeformed position of the filter.
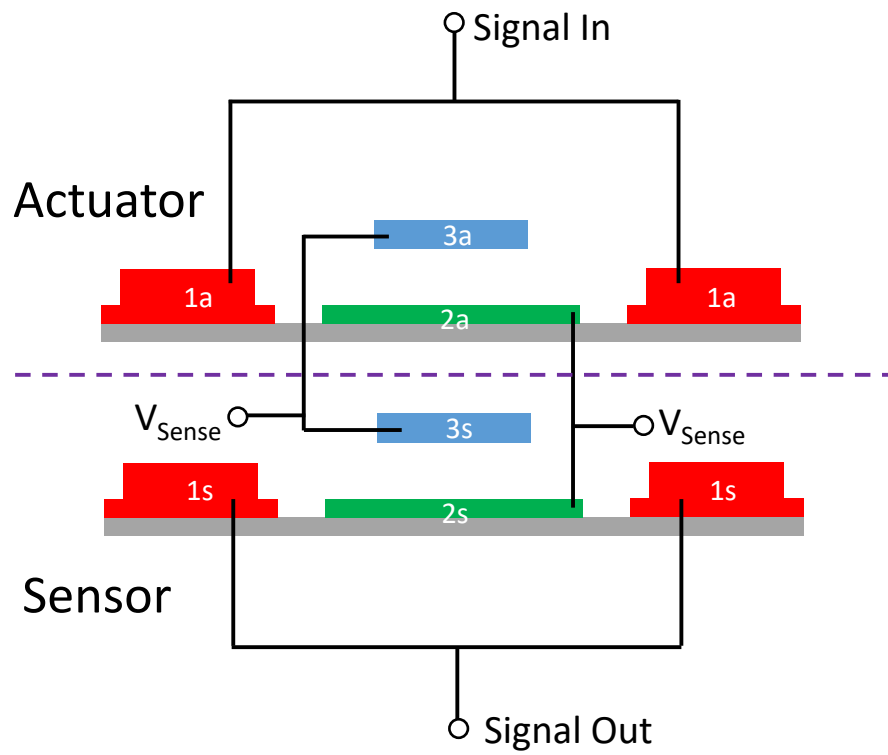
Figure 4: Electrical connections to the filter. $V_{sense}$ is the voltage used for capacitive sensing. In this case, it is also used to boost the motion of the actuator, and shield the output signal from being distorted by the input signal.
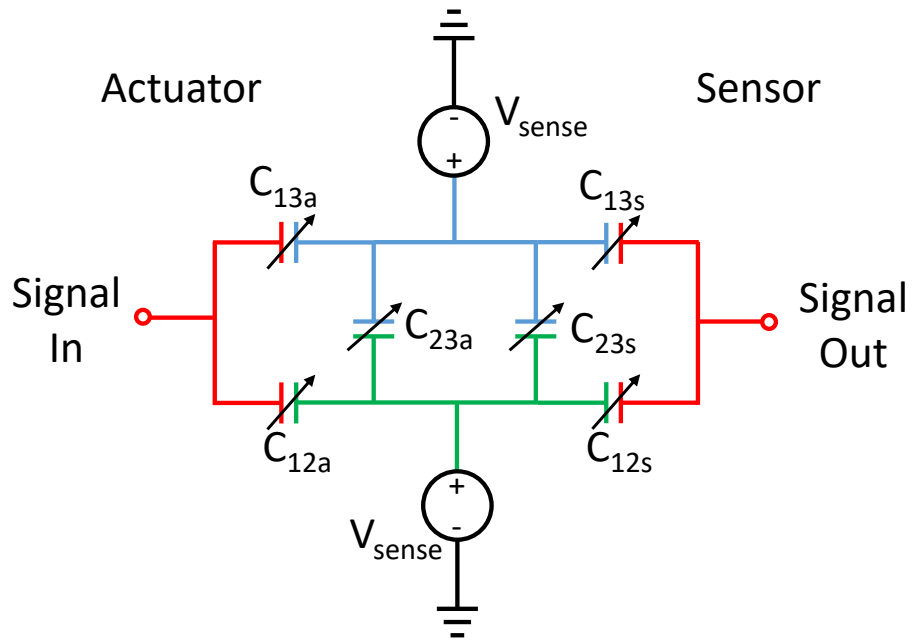
Figure 5: Equivalent circuit of the filter. The wire colors and numbers correspond to the electrodes in Figure 4.
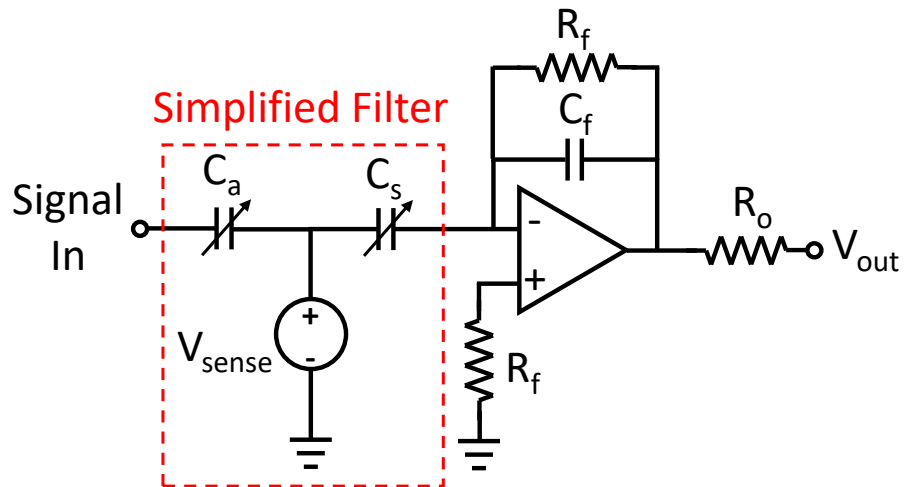


Figure 6: Simplified filter circuit (red box) connected to a charge amplifying circuit.
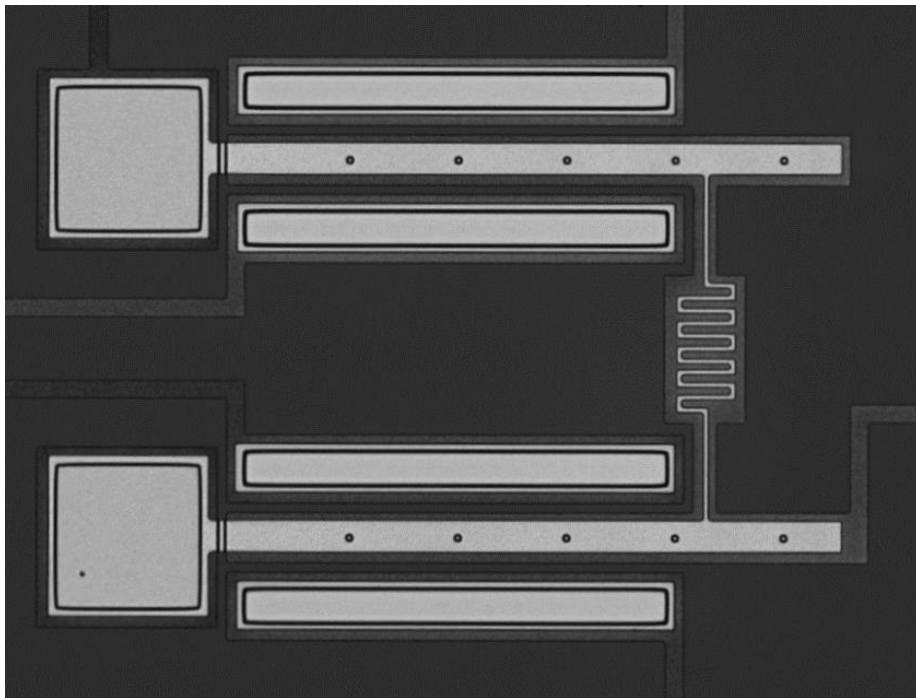
Figure 7: Optical image of a fabricated filter.
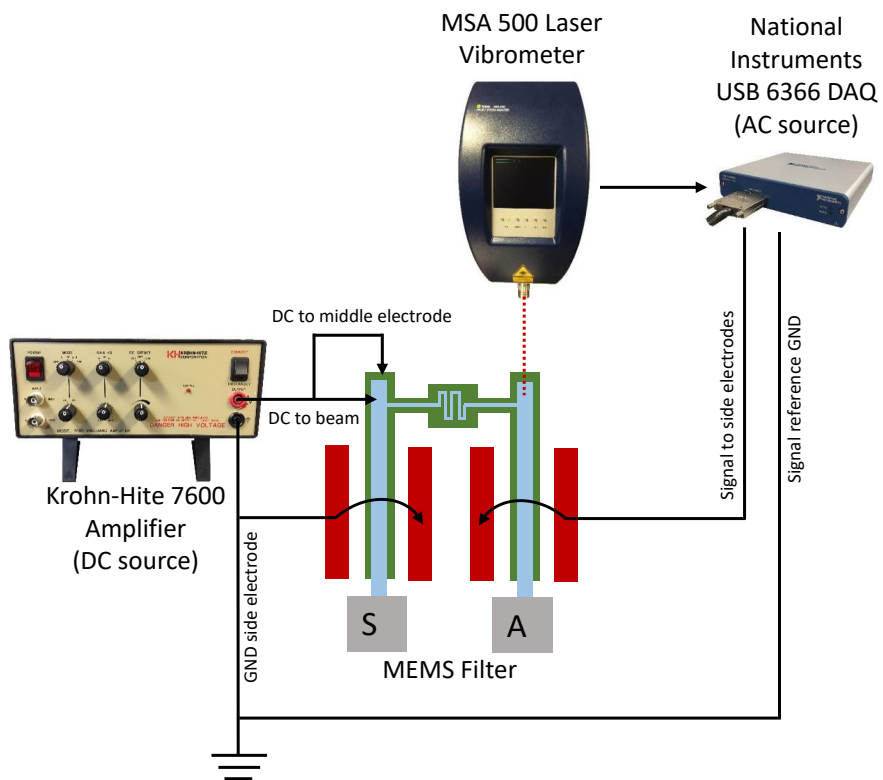
Figure 8: Experimental setup for the mechanical characterization of the filters.
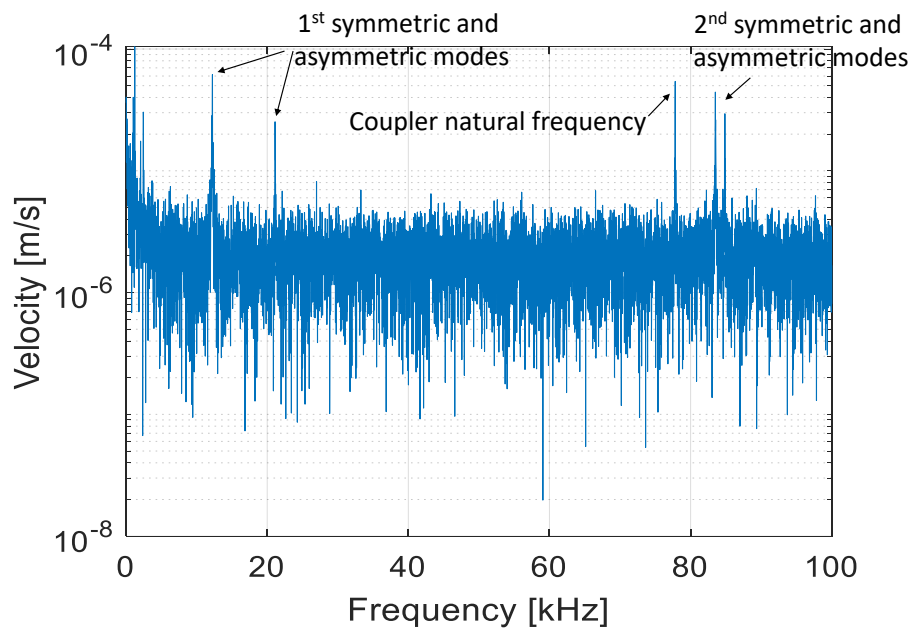
Figure 9: FFT of the actuator tip velocity when excited by a small white noise signal and no DC voltage. The spikes show the natural frequencies of the filter.
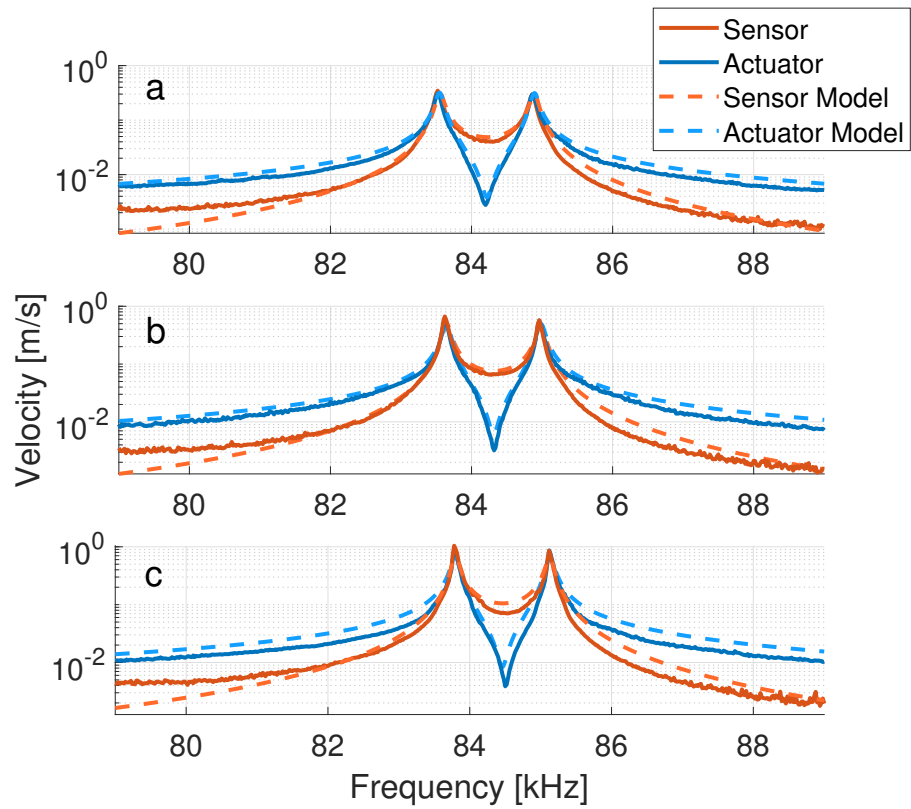
Figure 10: Frequency response of the sensing and actuating beam at $0.75V_{AC}$ and a $V_{DC}$ of a) 50V, b) 75V, and d) 100V. Both model and experiment show excellent agreement with each other.
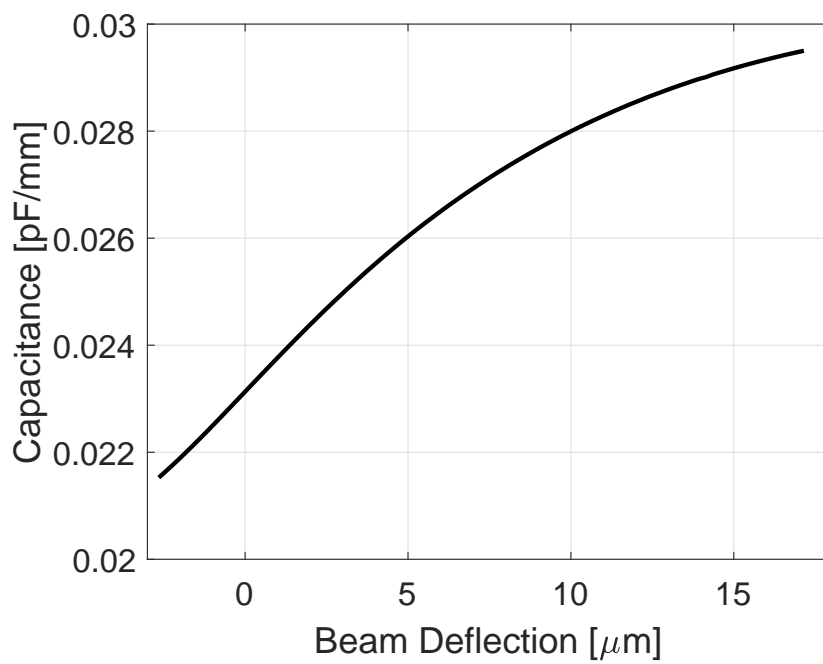
Figure 11: Capacitance per unit length between the center electrode/beam and side electrodes. This is the equivalent capacitance for both $C_a$ and $C_s$ in Figure 6
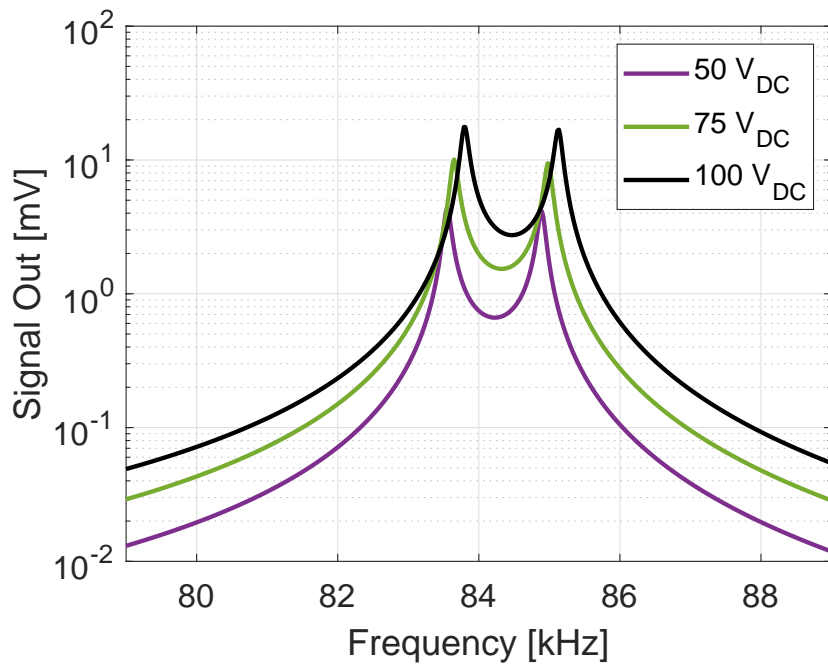
.

Figure 12: Calculated peak-to-peak signal out from the filter circuit in Figure 6 using Eq. (1) for $0.75V_{AC}$ and a sense voltage of 50V, 75V, and 100V. The feedback capacitor ($C_f$) is assumed to be 1pF.

.